INSTITUTE OF PHYSICS PUBLISHING and INTERNATIONAL ATOMIC ENERGY AGENCY NUCLEAR FUSION

Nucl. Fusion **44** (2004) 320–328 PII: S0029-5515(04)73460-2

ELMs and constraints on the H-mode pedestal: peeling–ballooning stability calculation and comparison with experiment

P.B. Snyder[1], H.R. Wilson[2], J.R. Ferron[1], L.L. Lao[1], A.W. Leonard[1], D. Mossessian[3], M. Murakami[4], T.H. Osborne[1], A.D. Turnbull[1] and X.Q. Xu[5]

[1] General Atomics, PO Box 85608, San Diego, CA 92186-5608, USA
[2] EURATOM/UKAEA Fusion Association, Culham Science Centre, Abingdon, Oxon UK
[3] Massachusetts Institute of Technology PSFC, Cambridge, MA 02139, USA
[4] Oak Ridge National Laboratory, Oak Ridge, Tennessee, USA
[5] Lawrence Livermore National Laboratory, Livermore, CA 94550, USA

E-mail: snyder@fusion.gat.com

Received 7 November 2002, accepted for publication 4 December 2003
Published 16 January 2004
Online at stacks.iop.org/NF/44/320 (DOI: 10.1088/0029-5515/44/2/014)

Abstract
We review and test the peeling–ballooning model for edge localized modes (ELMs) and pedestal constraints, a model based upon theoretical analysis of magnetohydrodynamic (MHD) instabilities that can limit the pedestal height and drive ELMs. A highly efficient MHD stability code, ELITE, is used to calculate quantitative stability constraints on the pedestal, including constraints on the pedestal height. Because of the impact of collisionality on the bootstrap current, these pedestal constraints are dependent on the density and temperature separately, rather than simply on the pressure. ELITE stability calculations are directly compared with experimental data for a series of plasmas in which the density is varied and ELM characteristics change. In addition, a technique is developed whereby peeling–ballooning pedestal constraints are calculated as a function of key equilibrium parameters via ELITE calculations using series of model equilibria. This technique is used to successfully compare the expected pedestal height as a function of density, triangularity and plasma current with experimental data. Furthermore, the technique can be applied for parameter ranges beyond the purview of present experiments, and we present a brief projection of peeling–ballooning pedestal constraints for burning plasma tokamak designs.

PACS numbers: 52.35.Py, 52.55.Tn, 52.65.Kj, 52.55.Fa

1. Introduction and motivation

High performance ('H-mode') operation in tokamaks is characterized by the spontaneous formation of a transport barrier near the edge of the closed flux surface region. The term 'pedestal' is used here to describe the resulting sharp pressure gradient region just inside the magnetic separatrix in H-mode operation. This region generally occupies approximately the outer 1–5% of the normalized radius of the closed flux surface region but is observed to have a disproportionately large impact on overall plasma performance (see, e.g. [1–3]).

The physics of the pedestal is important to the performance of present tokamak experiments and is expected to be critically important for future burning plasma devices for two primary reasons. The first is the strong dependence, both observed and predicted by transport models, of core confinement on the pressure at the top of the pedestal (or 'pedestal height'). Core transport models generally take the pedestal height as an input parameter and predict the resulting transport in the core plasma. Because these models are generally 'stiff' (transport increases rapidly above a critical gradient), the predicted core temperature, and hence fusion power or $Q = P_{\rm fus}/P_{\rm in}$, increases strongly with increasing pedestal height. For GLF23, the dependence is roughly $P_{\rm fus} \sim \beta_{\rm ped}^2$, where $\beta_{\rm ped}$ is the ratio of plasma to magnetic pressure at the top of the pedestal [4]. Hence, transport code predictions for proposed burning plasma candidates can be restated in terms of the pedestal height

(or at a given density, the pedestal temperature) requirements for a given level of fusion performance.

The second important pedestal physics issue is the presence of edge localized modes (ELMs). ELMs are repetitive magnetic perturbations in the pedestal vicinity, which transport bursts of particles, and usually also heat, across the separatrix and to the divertor plates (see, e.g. [5–9]). While the ELMs themselves are generally benign in present experiments, large ELMs potentially pose a significant divertor erosion risk in burning plasma scale devices. Furthermore, as discussed below, ELMs appear to be a manifestation of magnetohydrodynamic (MHD) instabilities driven by a combination of the strong pressure gradient and resulting bootstrap current in the pedestal region. These instabilities place constraints on the achievable pedestal height at a given transport barrier width and thus constrain overall performance as discussed above. Developing a predictive understanding of the physics controlling ELMs and the pedestal height is thus an important objective for pedestal theory, with a goal of maximizing the pedestal height while maintaining acceptable ELM behaviour.

1.1. Background: pedestal MHD stability and the ELITE code

The sharp pressure gradients, and consequent large bootstrap currents in the pedestal region, can destabilize peeling (i.e. edge localized external kink) and ballooning modes over a wide range of toroidal mode numbers (n). The bootstrap current plays a complex dual role in the stability physics, on one hand driving peeling modes, while on the other hand lowering edge shear and opening second stability access to high-n ballooning modes. Field line bending stabilizes long wavelength modes, while short wavelengths are stabilized by a combination of second stability and FLR/diamagnetic effects, shifting the limiting modes to intermediate wavelengths (typically $n \sim 4$–40). These dominant modes are referred to here as coupled 'peeling–ballooning' modes and are driven by both parallel current (J_{ped}) and the pressure gradient (p'_{ped}) [10, 11]. These intermediate-n peeling–ballooning modes impose constraints on the pedestal height, which are functions of the pedestal width, plasma shape, collisionality, safety factor and other equilibrium details.

A new MHD stability code, ELITE [12, 11], employs a novel finite-n extension of ballooning theory [12] that allows accurate and highly efficient study of $5 \lesssim n \lesssim 100$ peeling–ballooning modes in shaped toroidal geometry. ELITE calculates both growth rates (compressionless or compressional) and mode structures of the limiting instabilities, which provide useful input for the development of ELM models. ELITE uses a Fourier representation in the poloidal direction and employs numerical methods that allow very efficient stability calculations, facilitating its use in the large number of stability calculations that are needed to characterize pedestal stability constraints as a function of mode wavelength, pedestal width, plasma shape, collisionality, safety factor, etc. A sample ELITE benchmark is shown in figure 1, where growth rates from ELITE are compared at lower n's with growth rates from the GATO [13] code, and calculated mode structures are also compared. ELITE, together with low-n MHD codes such as GATO, allows quantitative study of the full relevant spectrum of n.

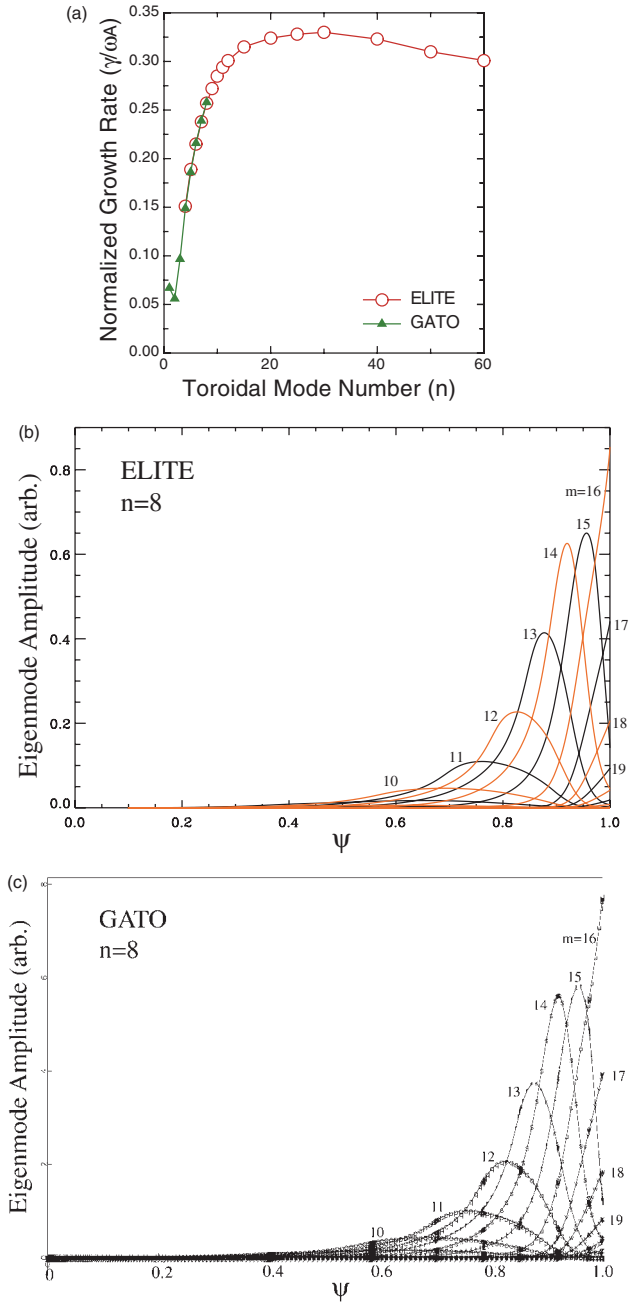

Figure 1. (*a*) Growth rates from the ELITE and GATO codes for a circular benchmark case show good agreement in the range of overlap ($4 \leqslant n \leqslant 9$). Calculated eigenmode structures from (*b*) ELITE and (*c*) GATO are also compared. The relative amplitudes and radial structure for the various poloidal modes are shown here for $n = 8$.

ELITE results together with analytic insights are used to develop a model of various types of ELMs and stability constraints on the pedestal, including direct constraints on the pedestal temperature (T_{ped}) [14]. Basic aspects of the model are described in figure 2 [11]. Quantitative stability limits are calculated by varying the pedestal temperature and density while self-consistently calculating the current,

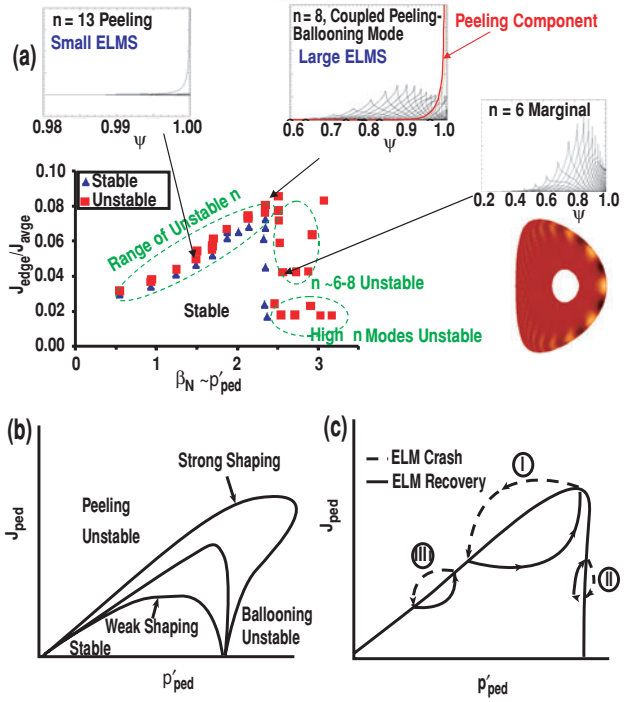

Figure 2. (*a*) Calculated pedestal stability boundary for $5 < n < 30$, along with eigenmodes of the limiting instability in various regimes. A two-dimensional contour plot of an $n = 6$ mode structure is inset. (*b*) A schematic showing the variation of pedestal stability boundaries with discharge shaping. (*c*) Model of three types of ELM cycle.

including bootstrap contributions. Figure 2(*a*) shows such limits for a JET-like equilibrium with fixed profile shapes. The stability boundary in J_{ped}, $\beta_N(\beta_N \propto p'_{ped})$ space is shown for the range $5 < n < 30$, along with eigenmode structures of the limiting instability in various regimes. Peeling modes are the limiting instability at high J_{ped}, low p'_{ped}, while ballooning modes are most unstable at high p'_{ped}, low J_{ped}. Intermediate $6 < n < 8$ coupled peeling–ballooning modes are the limiting instability in the high p'_{ped}, high J_{ped} region in which high performance shots generally operate.

Because of the strong collisionality dependence of the bootstrap current, there is generally a monotonic relationship between the pedestal temperature and J_{ped} in the regime of interest. Hence, diagrams like figure 2(*a*) can be recast into stability limits in p'_{ped}, T_{ped} space and used to calculate direct stability limits on the pedestal temperature at a given pedestal width. The pedestal stability boundary is a strong function of discharge shape, as shown schematically in figure 2(*b*). Improving shaping, for example by increasing triangularity, decouples peeling and ballooning modes, opening up second stability access for high-n modes and leading to a stability boundary at higher p'_{ped}, J_{ped} (and hence higher T_{ped}). Note the rather complex dependences depicted in figure 2(*b*). For example, while increasing current is always destabilizing for the 'weakly shaped' case, it can be strongly stabilizing in a 'strongly shaped' case where a higher current lowers the shear and opens second stability access to high-n modes, resulting in a higher stability boundary in p'_{ped} and a longer wavelength limiting instability.

Models for various ELM cycles can be envisioned in this p'_{ped}, J_{ped} parameter space, as shown in figure 2(*c*). Dynamically, the pressure gradient increases on a transport timescale, while the current grows on a slower resistive timescale, and an intermediate-n peeling–ballooning mode is triggered when the stability boundary is reached at the upper right of the diagram, resulting in a Type I ELM. Smaller ELMs are expected when the current, due to a combination of high collisionality and/or increased stability limit due to strong shaping, does not reach the peeling–ballooning limiting value, even in the steady state but instead reaches the pure ballooning limit. This small ELM cycle is labelled 'II' in figure 2(*c*) (though the observed small ELMs we propose may be associated with this cycle are in some cases referred to as 'small Type I' ELMs and sometimes as 'Type II'). At low power and low density, the small ELM cycle labelled 'III' occurs, associated with striking the pure peeling limit (note that high density Type III ELMs are generally thought to be resistive modes and are not considered here). The ELM model takes the lost ELM energy to be related to the radial width of the calculated most unstable mode, and this, along with the location in parameter space at which the instability occurs, provides an explanation for large observed variations in ELM behaviour. Of course nonlinear ELM physics and scrape-off-layer (SOL) transport must be considered for the development of a fully quantitative theory of ELM heat loads to the divertor.

2. Comparison with experiment and projection to future devices

The peeling–ballooning stability model can be compared with experimental results in two ways: (1) via direct comparison with detailed equilibrium reconstructions of particular experimental shots, as described in section 2.1, and (2) via comparison of the broad experimental database with stability trends predicted using series of model equilibria that systematically vary pedestal parameters. A comprehensive technique allowing quantitative comparisons of peeling–ballooning stability limits on the pedestal height with experimental observations is described in section 2.2, along with studies of pedestal height as a function of density, triangularity and plasma current. Series of model equilibria can also be used to predict pedestal constraints in future machines, as described in section 2.3.

2.1. Direct comparisons to experiment

Recent advances in high resolution pedestal diagnostics allow progressively more detailed comparisons of the model with a range of experimental measurements. For example, a recent case study [11] of DIII-D H-mode shot 97887 found that the observed onset time of the ELMs is consistent with the time at which ELITE stability calculations find that peeling–ballooning modes become unstable with a significant growth rate. It was further found that the radial and poloidal structure of the peeling–ballooning eigenmode is qualitatively in agreement with estimates of the radial penetration depth of the ELM using Thomson data [11], and with observations in divertor balance experiments [15] that the ELM pulse is localized on the outboard side. Analysis of Alcator C-Mod

discharges has similarly shown that ELMs emerge when peeling–ballooning modes go significantly unstable, while 'enhanced D-alpha' and ELM-free shots are generally stable to peeling–ballooning modes [17]. JT-60U discharges have also been studied, and 'giant' ELMs are found to correlate with broad peeling–ballooning instabilities, while 'grassy' ELMs are driven by instabilities with a narrower mode structure [18]. Here, we extend previous studies with a detailed study of three DIII-D discharges in which the density is varied and ELM size is observed to decrease with density.

It has been consistently observed in several tokamaks that both the pedestal pressure and the size of ELMs are reduced as density is increased (e.g. [16]). To compare this observation with the stability model, experimental DIII-D equilibria are reconstructed at times shortly before an observed ELM for low (shot 105999, $n_{\rm eped} \sim 2 \times 10^{19}\,{\rm m}^{-3}$), medium (106005, $n_{\rm eped} \sim 4\times10^{19}\,{\rm m}^{-3}$) and high (106007, $n_{\rm eped} \sim 6\times10^{19}\,{\rm m}^{-3}$) density cases. Stability and predicted mode structure are then calculated with ELITE. Normalized growth rates as a function of toroidal mode number are shown in figure 3. In each case, the growth rate has reached a significant value shortly before the ELM occurs, again consistent with peeling-modes triggering the ELM, even though the high density case has a significantly lower pedestal pressure. The most unstable wavelength, defined to be the wavelength with the largest growth rate normalized to the diamagnetic frequency (which for a given case is proportional to $n\omega_{\rm A}$), decreases with density as shown in figure 3(*a*). The numerical values of the growth rates can be determined from figure 4(*a*) using the values of $\omega_{\rm A} = 2.6 \times 10^6\,{\rm s}^{-1}$, $2.2 \times 10^6\,{\rm s}^{-1}$ and $1.6 \times 10^6\,{\rm s}^{-1}$ for the low, medium and high density cases, respectively. Note that the MHD growth rates are of the order of $10^5\,{\rm s}^{-1}$ for all three cases, and estimated effective growth times as the pedestal is pushed across the stability boundary (see [22]) are of the order of $10^4\,{\rm s}^{-1}$. Furthermore, the radial width of the most unstable mode decreases with density as shown in figures 3(*b*)–(*d*). This decrease in mode width and increase in most unstable wavelength with density is due to a combination of a decrease in pedestal width and a decrease in the bootstrap current. Both the mode narrowing and the higher wavelength of the instability lead to the expectation of smaller ELMs at high density, in agreement with observation. However, we again

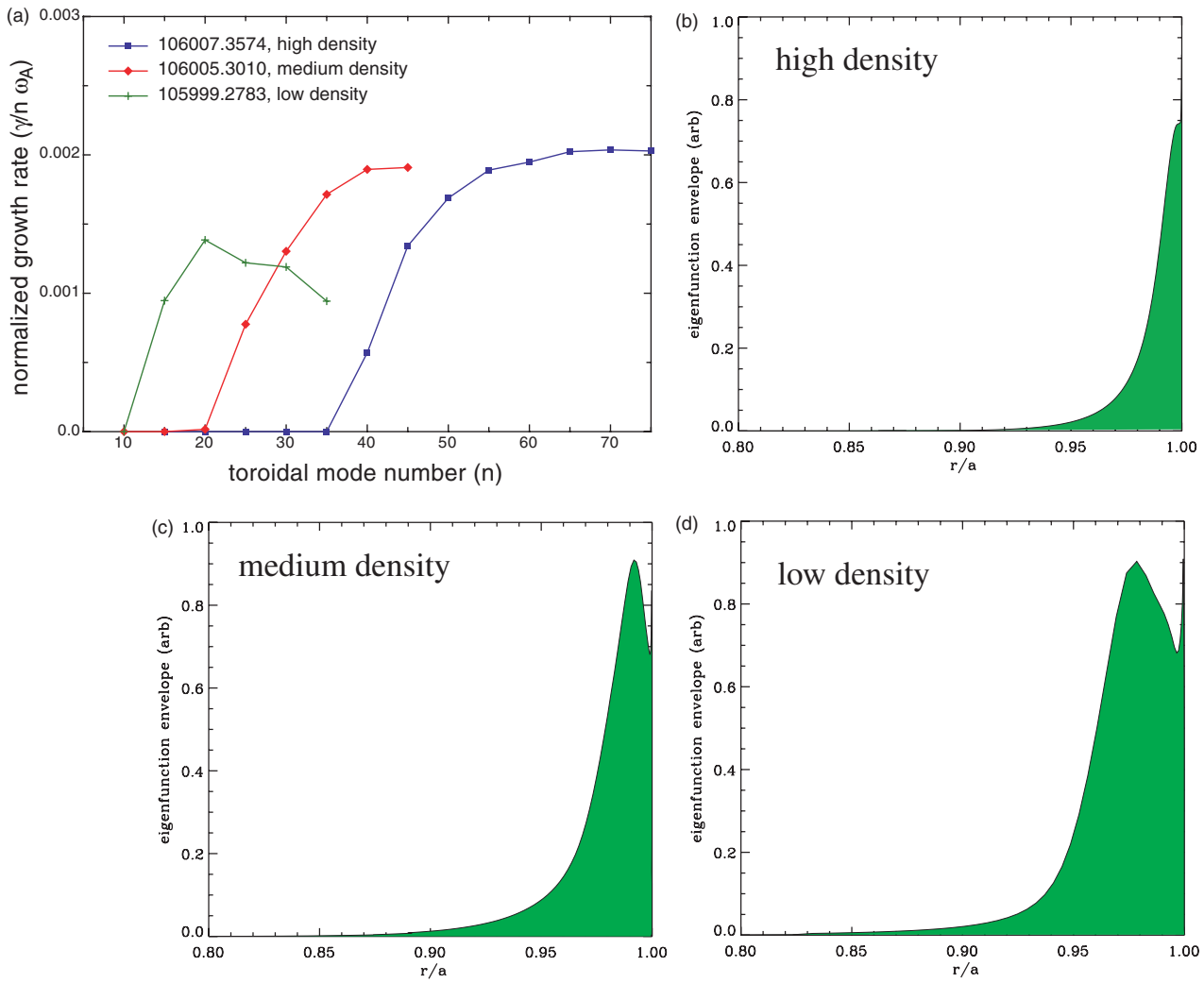

Figure 3. (*a*) Normalized growth rate vs n for DIII-D shots at high (106007), medium (106005) and low (105999) density, at times shortly before an ELM is observed. As density increases, the unstable spectrum peaks at shorter wavelengths. The eigenfunction envelope of the mode with largest normalized growth rate is shown for the same (*b*) high, (*c*) medium and (*d*) low density cases.

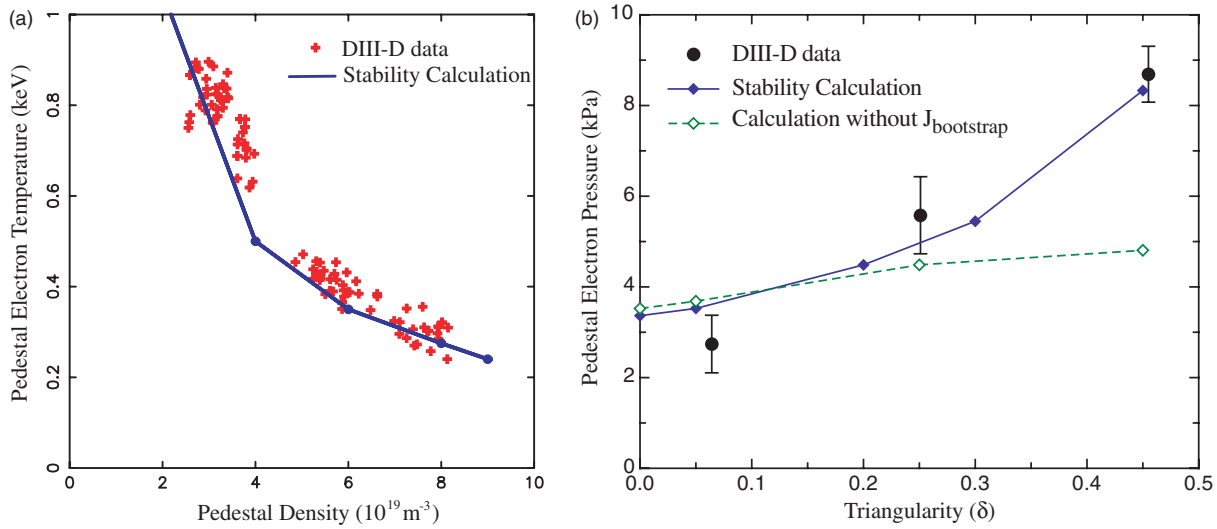

Figure 4. Comparison of calculated pedestal stability boundaries with observed trends in the DIII-D database. (*a*) The calculated maximum stable pedestal temperature as a function of density (solid line), is compared with the observed variation in pedestal temperature with density during the last 20% of the ELM cycle. (*b*) The calculated maximum stable pedestal pressure as a function of triangularity (——) is compared with the range of data (●). The calculated stability boundary with the bootstrap current artificially set to zero is shown by the dashed line.

emphasize that precise quantification of ELM size likely requires a detailed study of ELM and SOL dynamics. The narrowing of the linear eigenfunction of the most unstable mode is suggested as a possible qualitative contributing factor to the dynamical process that results in smaller ELMs at a higher density.

2.2. *Comparisons with experiment using model equilibria*

The comparisons with experiment described in the previous section provide rigorous tests of the ELM model and useful interpretive information on pedestal and ELM behaviour in experiments. However, such comparisons require detailed equilibrium reconstructions and thus can most easily be applied to the interpretation of existing experiments rather than to prediction of behaviour in present or future devices.

In order to systematically predict pedestal trends, both in present and future devices, we construct series of model equilibria, varying important pedestal stability parameters, and calculating MHD stability with ELITE.

Model equilibria are constructed to match expected or measured global parameters, including the toroidal magnetic field (B_t), total plasma current (I_p), major radius (R), minor radius (a), average electron density ($\langle n_e \rangle$), plasma elongation (κ) and triangularity (δ). Density and temperature profiles are given a hyperbolic tangent shape in the pedestal (resembling measured profiles (see, e.g. [3, 1])), and a simple polynomial dependence in the core:

$$n_e(\psi) = n_{sep} + a_{n0}\left\{\tanh\left[\frac{2(1-\Psi_{mid})}{\Delta}\right] - \tanh\left[\frac{2(\Psi-\Psi_{mid})}{\Delta}\right]\right\} + a_{n1}H\left(1-\frac{\Psi}{\Psi_{ped}}\right)\left[1-\left(\frac{\Psi}{\Psi_{ped}}\right)^{\alpha_{n1}}\right]^{\alpha_{n2}}$$

$$T(\psi) = T_{sep} + a_{T0}\left\{\tanh\left[\frac{2(1-\Psi_{mid})}{\Delta}\right] - \tanh\left[\frac{2(\Psi-\Psi_{mid})}{\Delta}\right]\right\} + a_{T1}H\left(1-\frac{\Psi}{\Psi_{ped}}\right)\left[1-\left(\frac{\Psi}{\Psi_{ped}}\right)^{\alpha_{T1}}\right]^{\alpha_{T2}}$$

where Ψ is the normalized poloidal flux, Δ is the pedestal width in Ψ space and H is the Heaviside step function. The constants a_0 and a_1 are chosen to give the desired pedestal and axis values, and α_1 and α_2 are chosen to approximately match expected core profiles from measurements or transport codes. Here we use $n_{ped} = 0.71\langle n_e \rangle$, $n_0 = 1.1\langle n_e \rangle$, $n_{sep} = 0.3\langle n_e \rangle$, $\alpha_{n0} = 1$, $\alpha_{n1} = 0.5$, $\alpha_{T0} = 1$, $\alpha_{T1} = 2$, $\Psi_{mid} = 1 - \Delta/2$, $\Psi_{ped} = 1 - \Delta$. In the pedestal region, the parallel current is taken to be equal to the bootstrap current, as calculated using the Sauter collisional model [19]. In the core, where details of the current are relatively unimportant, the profile is taken to have a simple polynomial form, with coefficients chosen to give a central $q_0 = 1.05$ and the desired I_p. A number of simplifications are made to streamline the equilibrium construction process, including up–down symmetry (while matching the given separatrix elongation and triangularity) and lack of true X-points. Note that the lack of X-points is a potentially significant approximation due to the impact of X-points on the flux surface averaged magnetic shear profile near the separatrix. However, this effect is somewhat mitigated because most of the instabilities studied here have a predominantly ballooning structure and the field line pitch near the outer midplane is affected little by the presence of X-points. The impact of X-point geometry, particularly on modes with a significant peeling component, remains an important area for future study.

A first set of model equilibria is constructed to study trends in the pedestal temperature as the density is varied. To allow comparison with a number of shots in the DIII-D

database, values of $B_t = 2\,T$, $I_p = 1.225\,MA$, $R = 1.685\,m$, $a = 0.603\,m$, $\kappa = 1.77$, $\delta = 0.0$ are used. The pedestal width on the outboard midplane is taken to be 1.7 cm. The pedestal density is then varied from (2–9) $\times 10^{19}\,m^{-3}$, and at each value of the pedestal density, the pedestal temperature is increased until stability limits are reached. Pedestal stability is calculated using the ELITE code. A sampling of wavelengths, $n = 8, 10, 15, 20, 30, 40$, is studied over the range expected to be most unstable. A finite growth rate threshold ($\gamma/\omega_A > 0.01$) is used as a threshold for 'instability', eliminating slow growing modes unlikely to trigger ELMs. We note that the results presented here and in the following section required the production of more than 1000 high resolution two-dimensional equilibria and more than 6000 intermediate-n MHD stability calculations but that the efficiency of the ELITE code combined with modern workstation computers makes such calculations feasible. The calculated stability limits on T_{ped} as a function of n_{eped} are shown by the solid line in figure 4(a).

In order to compare the calculated stability curve with observations, we use the DIII-D pedestal database, which contains information on pedestal temperature, density and width from fits of high resolution Thomson data to a hyperbolic tangent function [3]. The database contains information on several thousand timeslices from numerous shots, which can then be appropriately filtered, to allow comparisons with trends calculated using model equilibria. Here we select timeslices that are in the final 20% of the Type I ELM cycle, with $B_t = 1.9$–$2.05\,T$, $I_p = 1.15$–$1.25\,MA$, $\delta < 0.2$, temperature and density pedestal widths between 1.2 and 2.2 cm and injected power $P_{inj} > 1\,MW$. The data are plotted in figure 4(a), and provide a reasonable fit to the calculated stability limits, suggesting both that the pedestal is limited by MHD stability in the experiments and that the model equilibria are sufficiently realistic to capture the observed trends.

It is also of interest to study how the pedestal height varies with plasma shape, for example the triangularity (δ). For this purpose, we construct a set of model equilibria with $B_t = 2.08\,T$, $I_p = 1.525\,MA$, $\kappa = 1.8$, $n_{eped} = 4 \times 10^{19}\,m^{-3}$ and temperature and density pedestal width 1.4 cm. The triangularity is then varied from 0 to 0.45, and at each value, the pedestal temperature is increased until stability limits, calculated as in the previous case, are reached. The resulting stability boundary is plotted in figure 4(b). The result is again compared with filtered data, here with $B_t = 2.05$–$2.15\,T$, $I_p = 1.4$–$1.65\,MA$, $n_{eped} = (3.5$–$4.5) \times 10^{19}\,m^{-3}$ and temperature and density pedestal widths between 0.9 and 1.9 cm. The data set consists of two low triangularity ($\delta = 0.0643 \pm 0.0005$) points with $p_{eped} = 2.75 \pm 0.63\,kPa$, 183 intermediate triangularity points ($\delta = 0.251 \pm 0.005$) with $p_{eped} = 5.58 \pm 0.85\,kPa$ and four high triangularity points ($\delta = 0.455 \pm 0.004$) with $p_{eped} = 8.69 \pm 0.57\,kPa$, where values are given in the form mean $\pm$ standard deviation. The observed strong increase in pedestal pressure with triangularity is consistent with the stability calculations. Physically, the stability limit increases due to increasing second stability access to high-n modes as shown schematically in figure 2(b), with the most unstable mode dropping from $n \gtrsim 40$ at $\delta = 0$ to $n \sim 10$ at $\delta = 0.45$. The role of the bootstrap current is crucial here. In the absence of bootstrap current, second stability access is not opened and the increase in maximum stable pedestal pressure with triangularity is much weaker, as shown by the dashed line in figure 4(b). We note that this result is consistent with the observed trend that at high collisionality, where the bootstrap current is strongly reduced, the variation in pedestal height with triangularity is observed to be much weaker.

Finally, we present a study of the pedestal height as a function of total plasma current (I_p). For this study, we construct a set of model equilibria with $B_t = 2.075\,T$, $R = 1.69\,m$, $a = 0.59\,m$, $\kappa = 1.8$, $\delta = 0.25$. The pedestal width (Δ) is taken to be 4.5% of the normalized poloidal flux, and the pedestal density (n_{eped}) is taken to be 40% of the Greenwald limit (n_{GW}), where $n_{GW}(10^{14}\,m^{-3}) = I_p(MA)/\pi a^2(m)$. The current ($I_p$) is varied from 0.75 to 1.75 MA. Note that the current in the pedestal region remains bootstrap aligned while the core current is varied and that q_{95}, the safety factor at the 95% flux surface, decreases from 8.7 at $I_p = 0.75\,MA$ to 3.4 at $I_p = 1.75\,MA$. The pedestal temperature is increased at each value of I_p until the stability boundary is found. Here, ELITE is used to test stability for $5 < n < 30$, and the DCON code is used to confirm stability at low-n. The calculated stability boundary is given by the solid line in figure 5. Note that a roughly linear increase in the maximum stable pedestal pressure with current is seen over the studied range. In order to compare the calculated stability bound with data, we filter the DIII-D database for points within the last 20% of the Type I ELM cycle, with $2.05\,T < B_t < 2.1\,T$, $0.3 < n_{eped}/n_{GW} < 0.5$, $0.2 < \delta < 0.4$ and $3.5\% < \Delta < 5.5\%$. The mean value and standard deviation of the resulting data set are plotted as circles with verticle error bars in figure 5. The data set consists of 19 points with $I_p = 0.746 \pm 0.004\,MA$ and $p_{eped} = 3.20 \pm 0.69\,kPa$, 25 points with $I_p = 0.796 \pm 0.009\,MA$ and $p_{eped} = 3.55 \pm 0.47\,kPa$, 13 points with $I_p = 1.112 \pm 0.005\,MA$ and $p_{eped} = 5.00 \pm 0.31\,kPa$, 116 points with $I_p = 1.469 \pm 0.006\,MA$ and $p_{eped} = 6.35 \pm 0.91\,kPa$ and 27 points with $I_p = 1.564 \pm 0.004\,MA$ and $p_{eped} = 7.32 \pm 1.11\,kPa$, where values are given in the form mean$\pm$standard deviation. Good agreement is found between the calculated pedestal stability limit and

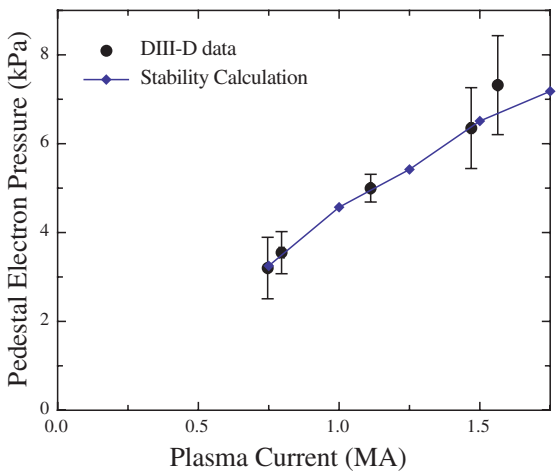

Figure 5. Comparison of calculated pedestal stability limit to observed pedestal height as a function of plasma current. The pedestal stability limit calculated using model equilibria is given by the solid line. Mean (●) and standard deviation (error bar) of the DIII-D data in the the last 20% of the Type I ELM cycle are shown.

the observed pedestal height shortly before an ELM, both in absolute value and in the trend with I_p.

In figures 4 and 5, there is of course significant variation in the observed data, even when filtered, as there are a number of parameters that are not tightly controlled by the limited filtering. Furthermore, the profile and shape details in the actual shots are only approximately captured in the model equilibria. However, it is quite encouraging that general trends in pedestal height appear to be predictable using model equilibria that approximately match the most important characteristics (e.g. B_t, I_p, $\langle n_e \rangle$, κ, δ, Δ) and a bootstrap current model for the pedestal current (which is not accurately measured in present experiments). This result encourages the use of this technique to project approximate pedestal constraints that are expected to pertain in Next Step burning plasma devices, as discussed in the following section.

2.3. Prediction of pedestal constraints in ITER and FIRE

The need to attain a high pedestal for good confinement, while operating with sufficiently small ELMs to mitigate erosion of plasma facing components, is especially important to the successful operation of planned burning plasma experiments such as ITER and FIRE. While uncertainty in pedestal transport, in particular the inability to predict the expected pedestal width, makes pedestal prediction challenging, the methods of the previous section can nonetheless be used to calculate the pedestal constraints imposed by stability as a function of the pedestal width and other plasma parameters.

Model equilibria are constructed as in the previous section with reference values of $B_t = 5.3\,\mathrm{T}$, $I_p = 15\,\mathrm{MA}$, $R = 6.2\,\mathrm{m}$, $a = 2.0\,\mathrm{m}$, $\kappa = 1.85$, $\delta = 0.49$ and $\langle n_e \rangle = 1.0 \times 10^{20}\,\mathrm{m}^{-3}$ for ITER and $B_t = 10\,\mathrm{T}$, $I_p = 7.7\,\mathrm{MA}$, $R = 2.14\,\mathrm{m}$, $a = 0.595\,\mathrm{m}$, $\kappa = 2.0$, $\delta = 0.7$ and $\langle n_e \rangle = 3.6 \times 10^{20}\,\mathrm{m}^{-3}$ for FIRE. To characterize the pedestal stability constraints, the pedestal width (Δ is varied, and at each value of Δ, the pedestal temperature is increased incrementally with the bootstrap current calculated self-consistently) until stability boundaries are crossed. Results are summarized in figure 6. Note that while the maximum stable pressure increases with pedestal width, the dependence is sub-linear, i.e. a higher gradient can be achieved for narrower pedestals. This is because finite-n modes are sensitive to the change in profiles across the pedestal, not just to the local gradient, and because shear increases as the width decreases. More details of the ITER/FIRE pedestal stability study, including studies of variation with triangularity and density, can be found in [20].

3. Summary and discussion

We review a model for ELMs and constraints on the pedestal based on MHD stability of intermediate wavelength peeling–ballooning modes, which are driven unstable by the sharp pressure gradient and resulting bootstrap current in the pedestal region. The current plays a key dual role in the stability physics, on the one hand providing drive for peeling modes, while on the other hand lowering magnetic shear and, in the presence of shaping, allowing access to second stability for short wavelength instabilities. Field line bending stabilizes long wavelength modes, while short wavelengths are stabilized by a combination of second stability and FLR/diamagnetic effects. As a result, peeling–ballooning mode of intermediate wavelengths (typically $n \sim 4$–40) are often the limiting instability. The peeling–ballooning stability constraints imposed on the pedestal height are separate functions of density and temperature due to the collisionality dependence of the bootstrap current and are in general strong functions of the plasma shape and pedestal width, though not simply linear with pedestal width.

An MHD stability code, ELITE, has been developed to allow efficient evaluation of stability bounds, growth rates and mode structures of intermediate wavelength instabilities in the pedestal region. ELITE calculations allow quantitative study of stability constraints on the pedestal and together with analytic insight lead to a model of various types of small and large ELM cycle.

Stability calculations on reconstructed experimental equilibria from multiple machines consistently find that peeling–ballooning mode growth rates rise to significant values just before ELMs occur [11, 15, 17, 18]. A detailed new study of DIII-D shots of varying density finds that the ELMs in all three cases are consistent with a peeling–ballooning mode trigger, and that decreases in radial mode width and increases in most unstable mode number with density are consistent, within the peeling–ballooning model, with the observed decrease in ELM size with density.

A key advancement described in this paper is the development of a technique that employs model equilibria and ELITE to calculate the peeling–ballooning stability constraint on the pedestal as a function of key equilibrium parameters (Δ, B_t, I_p, R, a, κ, δ, n_{eped}) as well as a few less important parameters needed to fully specify the equilibrium. Using this technique, calculations of the pedestal stability limit as a function of density, triangularity and plasma current are quantitatively compared with a large data set of observations from DIII-D. Generally good agreement is found both in the quantitative value of the pedestal height and in its trends with the varied parameters. The triangularity study also confirms the important role of the bootstrap current in pedestal stability.

Because this technique does not require experimental equilibrium reconstruction, it can be applied to make predictions for future experiments on existing and planned devices as well as comparisons with existing databases. As an example, we present a study of pedestal constraints in planned burning plasma experiments. A key uncertainty in such studies is that while most of the key equilibrium quantities are known or controllable (B_t, I_p, R, a, κ, δ, n_{eped}), the pedestal width is not known and there exists no well established first principles model. Predictions are thus given as a function of the width. We note that comparisons of pedestal stability studies with databases of observed pedestal height and width may be useful for separating the dependences between pedestal width and height that arise from stability constraints, from the dependences that arise due to the transport or other physics that determines the width.

A number of additional effects, including diamagnetic stabilization, sheared rotation and $E \times B$ flows, as well as nonlinear dynamics, should be considered for a fully quantitative model of ELMs and pedestal constraints. Simple models of diamagnetic stabilization (e.g. $\gamma_{MHD} > \omega_*/2$) can

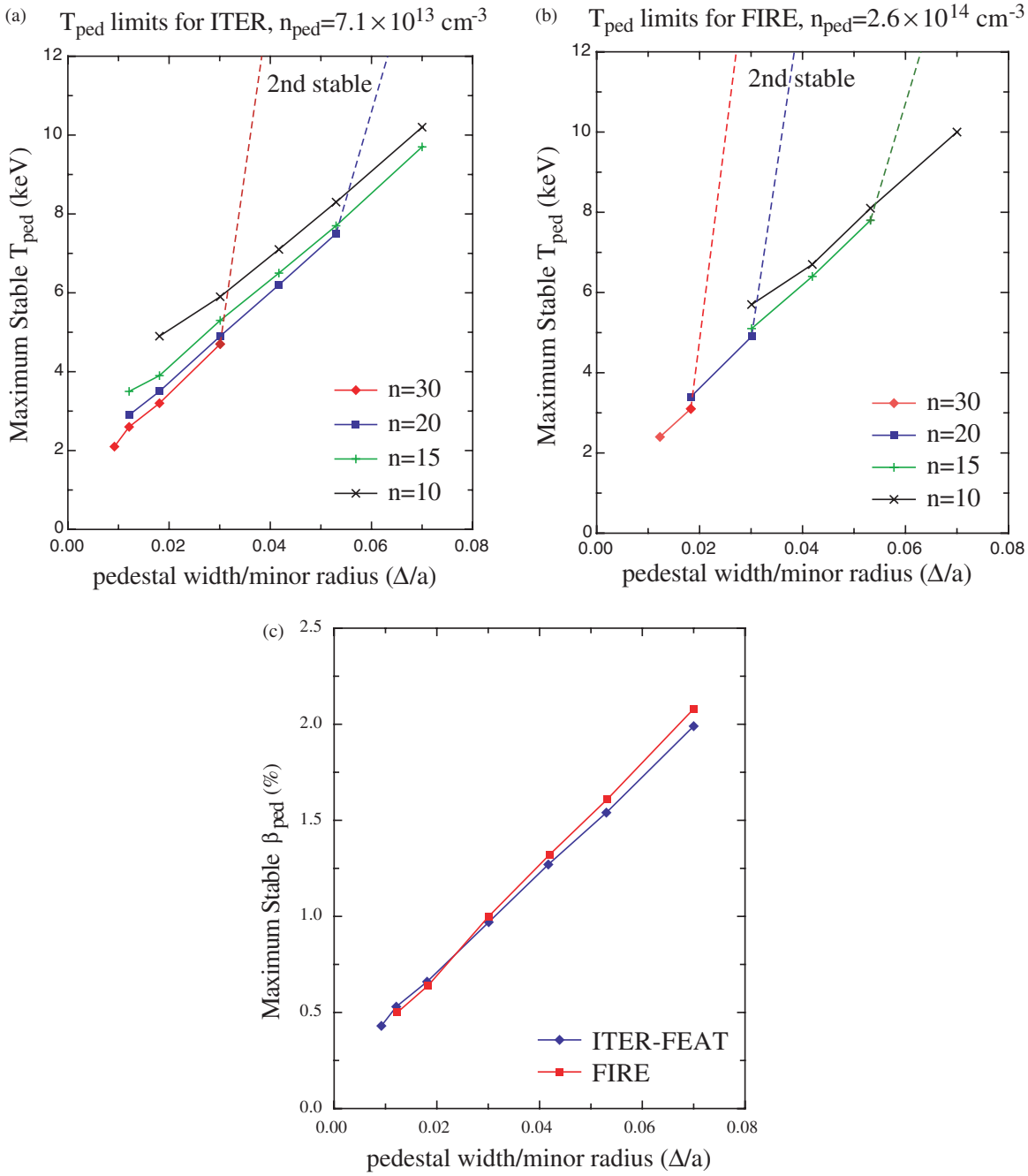

Figure 6. Maximum stable pedestal temperature as a function of normalized pedestal width shown for a range of mode numbers in (*a*) ITER and (*b*) FIRE. In both cases, high-*n* modes become second stable for wide pedestals. The dashed lines symbolically represent the transition of higher-*n* modes to second stability as the pedestal width increases above a critical value. (*c*) Comparison of ITER and FIRE pedestal stability limits in terms of the pedestal β.

be used to approximately assess its importance in various regimes [20]. Work is ongoing on including additional physics into ELITE, and simulations have been carried out with the nonlinear Braginskii-based BOUT code, with current added [21] to allow more physically complete understanding. Preliminary results suggest that the linear behaviour of peeling–ballooning modes is similar in ELITE and BOUT. It is expected that nonlinear simulation and continuing linear stability physics studies will provide the basis for development of quantitative models of ELM onset and dynamics, which can then be coupled to developing transport models to allow fully predictive modelling of the pedestal.

The level of agreement between the peeling–ballooning model and observations in both shot-by-shot comparisons and parameter scans is strongly encouraging and suggests that a database or parametric fit of pedestal stability constraints as a function of key parameters should be a useful predictive and interpretive tool. Key extensions planned for the model include adding additional physics, comparing with a broader range of experiments and developing a pedestal stability database.

Acknowledgments

Work supported by US Department of Energy under Grant DE-FG03-95ER54309 and Contracts DE-AC0399ER54463, W-7405-ENG-48 and DE-AC05-00OR22725 and by the UK Department of Trade and Industry and EURATOM.

References

[1] Hubbard A.E. 2000 *Plasma Phys. Control. Fusion* **42** A15
[2] Hatae T., Sugihara M. and Hubbard A.E. 2001 *Nucl. Fusion* **41** 285
[3] Osborne T.H. *et al* 2000 *Plasma Phys. Control. Fusion* **42** A175
[4] Waltz R.E. *et al* 2002 Performance of burning plasma experiments *Snowmass Meeting* http://web.gat.com/snowmass/working/mfe/physics/p4/
[5] Zohm H. 1996 *Plasma Phys. Control. Fusion* **38** 105
[6] Connor J.W. 1998 *Plasma Phys. Control. Fusion* **40** 191
[7] Suttrop W. 2000 *Plasma Phys. Control. Fusion* **42** A1
[8] Lao L.L. 2000 *Plasma Phys. Control. Fusion* **42** A51
[9] Snyder P.B. and Wilson H.R. 2002 *Contrib. Plasma Phys.* **42** 258
[10] Connor J.W. *et al* 1998 *Phys. Plasmas* **5** 2687
[11] Snyder P.B. *et al* . 2002 *Phys. Plasmas* **9** 2037
[12] Wilson H.R. *et al* 2002 *Phys. Plasmas* **9** 1277
[13] Bernard L.C. *et al* 1981 *Comp. Phys. Commun.* **24** 377
[14] Wilson H.R. *et al* 2001 Coupled peeling–ballooning modes: a model for ELMs and the temperature pedestal? *EPS (Madeira)*
[15] Petrie T.W. *et al* 2003 *Nucl. Fusion* **43** 910
[16] Leonard A.W. 2002 Acceptable ELM regimes for burning plasmas *Proc. 19th Int. Conf. on IAEA Fusion Energy 2002 (Lyon, 2002)* (Vienna: IAEA) CD-ROM file and http://www.iaea.org/programmes/ripc/physics/fec2002/html/fec2002.htm
[17] Mossessian D. *et al* 2002 *Plasma Phys. Control. Fusion* **44** 423–37
Mossessian D.A. *et al* 2003 *Phys. Plasmas* **10** 1720
[18] Lao L.L. *et al* 2001 *Nucl. Fusion* **41** 295
[19] Sauter O., Angioni C. and Lin-Liu Y.R. 1999 *Phys. Plasmas* **6** 2834
[20] Snyder P.B. and Wilson H.R. 2003 *Plasma Phys. Control. Fusion* **9** 1671
[21] Xu X.Q. *et al* 2002 *New J. Phys.* **4** 53
[22] Callen J.D. *et al* 1999 *Phys. Plasmas* **6** 2963